Journal of Atmospheric and Solar-Terrestrial Physics 78–79 (2012) 70–83

Contents lists available at ScienceDirect

Journal of Atmospheric and Solar-Terrestrial Physics

journal homepage: www.elsevier.com/locate/jastp

Nightglow imaging of different types of events, including a mesospheric bore observed on the night of February 15, 2007 from Tirunelveli (8.7°N)

V. Lakshmi Narayanan *, S. Gurubaran, K. Emperumal

Equatorial Geophysical Research Laboratory, Indian Institute of Geomagnetism, Tirunelveli 627011, India

ARTICLE INFO

Article history:
Received 5 November 2010
Received in revised form
19 July 2011
Accepted 27 July 2011
Available online 3 August 2011

Keywords:
Quasi-monochromatic gravity waves
Ripples
Mesospheric bores
Thermal and Doppler ducts

ABSTRACT

All-sky imaging observations on the night of February 15, 2007, from Tirunelveli (8.7°N), revealed a variety of short-period small-scale dynamical features comprising of atmospheric gravity waves, ripples and a mesospheric bore. A total of 11 wave events other than the convective ripple patches were identified. All the ripple features of wavelengths less than 10 km were found to propagate nearly in the same direction and they were frequent in the early part of the night. The presence of a dynamical ripple in all-sky images was also inferred. One of the identified events displayed steepening of the leading front and subsequent evolution into a mesospheric bore. Apart from these events, there were several 'quasi-coherent' features that were not clearly discernable for deduction of propagation velocities or wavelengths. In order to have a better understanding of these events, we used winds measured by co-located MF radar to derive intrinsic wave parameters. The MF radar winds and average of zenith intensity values from the imager indicate the presence of medium frequency waves of time periods in the range 0.75–3 h. In addition, two sets of temperature measurements made by SABER instrument onboard TIMED mission were also used. The temperature profiles implied strong tidal control on this night. An attempt was also made to infer the source of the wave activity observed at mesospheric altitudes and the effects of wind filtering at altitudes below nightglow emission altitudes.

1. Introduction

The mesopause region (80–100 km) is an interesting and complex regime in the Earth's atmosphere. This is a transition region above which electric and magnetic fields play an important role resulting in electrodynamical effects in the ionosphere and below which neutral atmospheric wave motions dominate the dynamics. The studies on the processes occurring in this region are very important for a better understanding of the atmosphere–ionosphere coupling. Though gravity waves constitute a dominant dynamical feature of this region (Hocking, 1996), there are still uncertainties in our knowledge on the percentage of those waves that propagate from the lower atmosphere to the upper mesosphere and those that are generated in the mesosphere and lower thermosphere region (MLT). The high frequency small-scale gravity waves carry large energy density when they propagate upwards and under certain conditions they can become ducted. Once ducted, they carry energy and momentum over large horizontal distances before breaking or dissipating at a distant location (Walterscheid et al., 1999). Such waves are believed to play an important role in determining the local state of the mesosphere.

All-sky imaging of the nightglow emissions is a unique technique that provides valuable information on horizontal wavelengths, phase velocities and propagation directions of small-scale gravity waves. Along with supplementary data on background wind and temperature, this technique can effectively be used towards a better understanding of dynamical processes occurring at the upper mesospheric altitudes. A variety of studies in the past utilized imaging observations to address small-scale gravity waves, instability features and unusual dynamical systems like bores and wall waves (Taylor et al., 1997; Swenson et al., 1998; Walterscheid et al., 1999; Nakamura et al., 1999; Smith et al., 2000; Hecht et al.,, 2001; Medeiros et al., 2001; Yamada et al., 2001; Shiokawa et al., 2003; Hecht, 2004; Brown et al., 2004; Li et al., 2005a, 2005b; Wrasse et al., 2006; Narayanan et al., 2010). In spite of such studies, it may be noted that a comprehensive understanding of the characteristics, distribution and interactions of high frequency small-scale gravity waves is still lacking.

In this work, our focus is on the gravity wave events and its associated dynamics observed with all-sky airglow imaging technique on the night of February 15, 2007, from the low latitude Indian site, Tirunelveli (8.7°N, 77.8°E). We have attempted to understand the dynamical activity around 87 km on this night with airglow imager, winds from co-located MF radar and two sets of temperature measurements made by Sounding of the Atmosphere with Broadband Emission Radiometry (SABER) instrument

* Corresponding author. Tel.: +91 462 2521465; fax: +91 462 2521466.
E-mail address: narayananvlwins@gmail.com (V. Lakshmi Narayanan).

1364-6826/$ - see front matter
doi:10.1016/j.jastp.2011.07.006

onboard the Thermosphere–Ionosphere–Mesosphere Energetics and Dynamics (TIMED) satellite. The schematic shown in Fig. 1 indicates the present observation location and a circle around the site represents an area covered by the 130° field-of-view of the imager at an altitude of 87 km. The locations over which SABER measurements (points joined by lines with arrows) were made on this night are also included in the schematic. The imaging observations reveal presence of high frequency (periods less than 0.5 h) waves, ripples associated with instability features and a mesospheric bore. From radar winds and zenith intensity values, we infer the presence of medium frequency waves (periods between 0.5 and 3 h).

We have utilized Outgoing Longwave Radiaton (OLR) data and cloud images from Kalpana 1 satellite to examine potential convective forcing agents for the events observed on this night. We use United Kingdom Meteorological Office (UKMO) assimilated winds up to stratopause height to probe the middle atmospheric filtering effects. No wind data were available to study wind filtering effects at lower mesospheric altitudes.

The observations on the night of February 15, 2007 reported herein are interesting for the following reasons: (1) The average number of wave-like features observed per night during the period January–February 2007 (winter months) was ~7 whereas the observations on February 15 showed presence of not less than 11 wave-like features (including a KH ripple). (2) Out of 14 nights of observations, observations on only three nights, namely, February 8, 15 and 16, revealed excessive wave activity that accounted for almost 40% of wave features observed during January and February 2007 campaigns. Moreover, of these three active nights, only February 8 and 15 showed presence of varied wave events, namely, quasi-monochromatic (QM) waves, ripples and bore-like fronts. (3) Imaging observations were made throughout the night on February 15, 2007 and also two sets of nearly coincident SABER temperature profiles are available for this night while the observations on the most active night, February 8, were hindered by moon rise during the later part of the night.

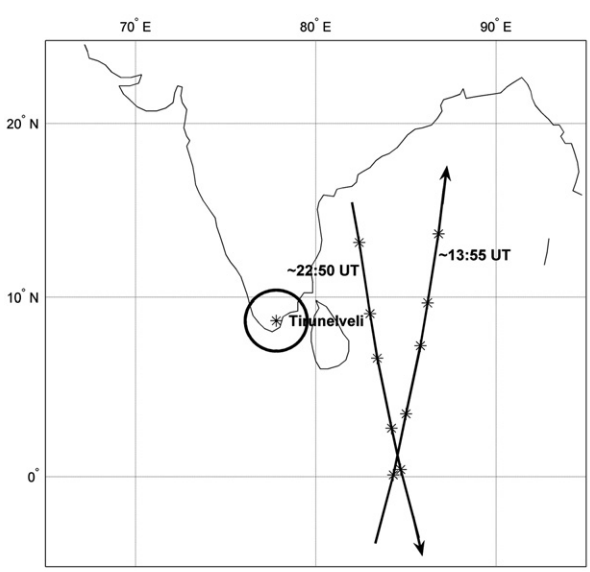

Fig. 1. Schematic depicting the observation location, Tirunelveli, with the circle indicating a field-of-view of 130°. The two lines marked with arrows represent the SABER measurement tracks on the night of February 15, 2007.

2. Data used and methodology

The imaging observations were carried out with four interference filters that covered the near-infra-red (NIR) region of OH Meinel bands, the OI 557.7 nm emission, the Na doublet emission and a background centered at 572.3 nm. The filter characteristics, the average altitude of the emissions and the exposure times chosen for the experiment are given in Table 1.

During every image acquisition, a set of images was acquired successively with each filter and the filters were changed in sequence. Successive images within a sequence were spaced at time gaps equal to the exposure time. Sequential acquisition enables us to obtain time-differenced (TD) images wherein successive images are differenced to yield time-differenced resultant images. Swenson and Mende (1994) cautioned on the emergence of pseudo-wave-like features in TD images, if proper care is not taken. In the present work it was ensured that the time difference between two successively acquired images was always less than 3 min, which is below the buoyancy time period. The retrieved wave parameters are consistent with those derived using the methods discussed in Garcia et al. (1997) and Narayanan et al. (2009b), wherein a resultant image was obtained when the observed image was subtracted from the average of several images acquired over a period. We did not find any arbitrary pseudo-wave-like features in our TD images. The TD method thus provided a suitable and convenient way of analyzing broadband OH Meinel images. As already pointed out by Swenson and Mende (1994), the phase velocities are reliably estimated in the TD method. In this work, we unwarped and projected the TD images onto an equidistant grid following the projection method described in Garcia et al. (1997).

Since the OH Meinel bands were observed with a broadband filter, the signal strength representing the airglow intensity observed with this filter was greater than that for other emissions. As a result, wave activity with more clarity could be observed in OH images than at other wavelengths and therefore in this work we address only those events recorded in OH images with the exception of a bore event. Since complementarity feature of mesospheric bores could not be studied with observations of one airglow emission, we analyzed observations of Na and OI 557.7 nm emissions as well as will be discussed later.

Table 1
Filter characteristics, exposure times of images and zenith spatial resolution at emission altitudes.

Emission wavelength (nm)	Assumed centroid altitude (km)	Filter peak transmission wavelength (nm)	Filter bandwidth (nm)	Peak Transmission (%)	Exposure times (s)	Spatial Resolution at emission altitudes (km)	
						Horizontal	Diagonal
OI (557.7)	97	557.8	1.79	53.5	180	0.57	0.81
Na (589 and 589.6)	90	589.2	1.98	71	180	0.53	0.76
OH meinel band	87	705.3–928.2 (notch ~865)	–	93.6	60	0.51	0.73
Background filter	–	572.3	1.95	84	180	–	–

Apart from measuring the parameters of quasi-monochromatic (QM) gravity waves and ripples observed by the imager, we derived zenith intensity values from the acquired raw images by taking average of a 13×13 pixel area in the center of every image. This is analogous to the operation of a narrow field-of-view photometer. Since the imager was not calibrated to yield intensities in Rayleighs, we present the intensity values in arbitrary photon counts recorded by the CCD.

The co-located MF radar at Tirunelveli with an operating frequency of 1.98 MHz yields information on winds at upper mesospheric altitudes. During the observation period, the winds were retrieved at every 2-km height intervals at 1.5-min time intervals. The wind estimates were based on the full correlation analysis methods as described by Briggs (1984). Further details of the instrument were provided in Rajaram and Gurubaran (1998). In order to overcome the data gap issues associated with 1.5-min data sets, we estimated 10-min averages of the winds measured at 86, 88 and 90 km altitudes. We used these averaged zonal and meridional winds for assessing the background wind condition and for examining long-period waves. Apart from this, hourly averages of winds were also used wherever necessary.

Fig. 2a and b shows the 10-min averaged and hourly averaged background winds, respectively. To obtain the intrinsic phase velocity of a wave, we estimated the duration over which the wave was observed and calculated the background wind along the wave propagation direction for the same duration from the 10-min averaged zonal and meridional wind data. The difference between the observed phase velocity and this background wind velocity gave the intrinsic phase velocity of the wave.

On this night, two sets of SABER measurements were available in the low latitude Indian sector as shown in Fig. 1. We used five successive profiles from each set to obtain representative background temperature profiles. The first set of measurements was made around 13:55 UT near the start of the nightglow observations and the second set around 22:50 UT near the end. Considering that the true vertical resolution of SABER measurements was ~2 km, we generated averages over 2-km altitudes from 0.4-km sampled data at 1-km sliding intervals (Narayanan et al., 2009a, 2010). Averages of five such profiles during the start and during the end of the observation period were estimated and they are considered to represent the background temperatures at these times. Fig. 3a shows the two mean temperature profiles for the altitude region of interest.

With the availability of temperature profiles, the static stability of the atmosphere could be inferred from profiles of square of buoyancy frequency (N^2) as given by the following expression:

$$N^2 = \frac{g}{T}\left(\nabla T_z + \frac{g}{C_p}\right) \quad (1)$$

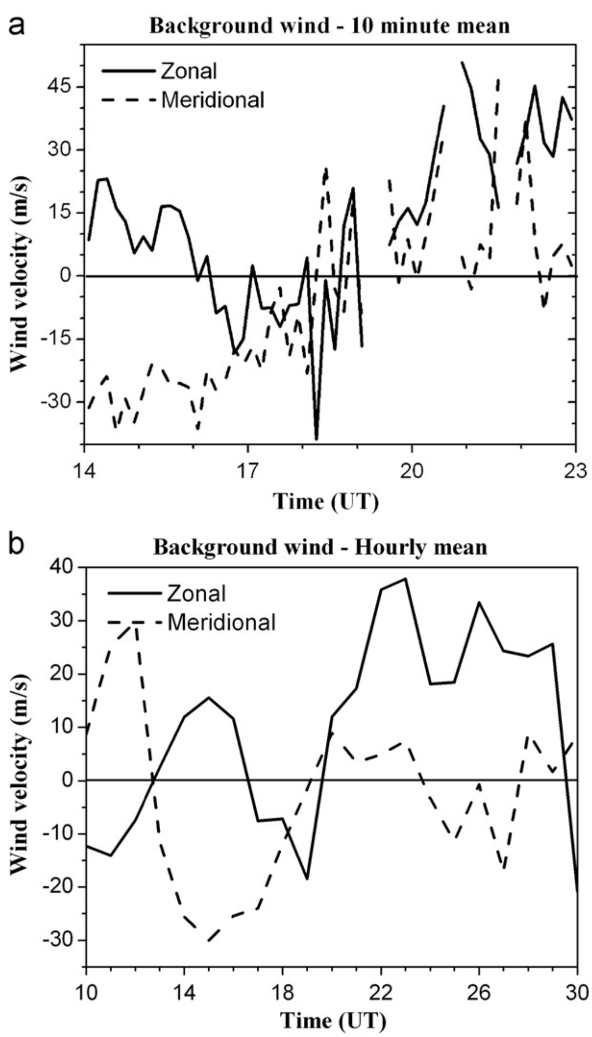

Fig. 2. Zonal and meridional winds averaged from 86, 88 and 90 km: (a) 10-min averages and (b) hourly averages.

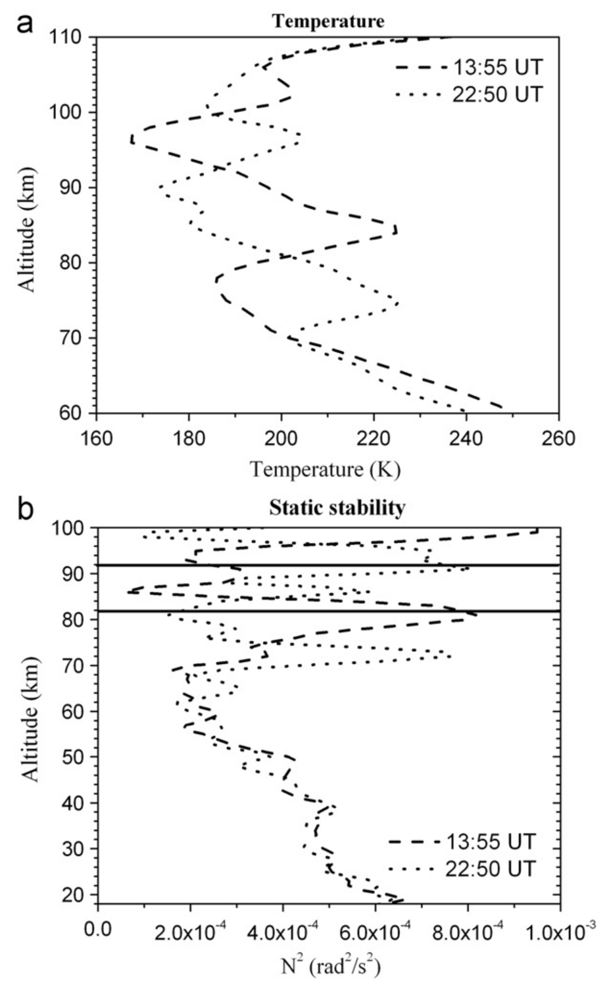

Fig. 3. (a) Background temperature profiles obtained by SABER at two different times on the night of February 15, 2007. (b) Profiles of square of buoyancy frequency (N^2) derived from measured SABER temperatures. The solid lines between 83 and 91 km show the region of OH nightglow.

The acceleration due to gravity, g, is taken as 9.54 ms^{-2} in the above equation with a specific heat $C_p = 1005$ J Kg^{-1} K^{-1}. T is the temperature and∇T_z is the vertical temperature gradient.

The derived static stability (N^2) profiles for the two temperature profiles for the altitude region 20–100 km are shown in Fig. 3b.

To examine the role of convective forcing in the generation of those gravity waves observed on this night, we utilized the daily Outgoing Longwave Radiation (OLR) data (available from http://iridl.ldeo.columbia.edu/SOURCES/.NOAA/.NCEP/.CPC/.GLOBAL/.daily/.olr/) along with the 3-hourly cloud images obtained from the Indian meteorological satellite Kalpana 1. Both data sets show similar features as will be discussed later. In order to assess wind filtering effects, we used UKMO assimilated winds available up to ~55 km. It may be noted that we do not have wind data in the lower mesospheric region to probe the filtering effects in that region.

3. Results and discussion

Before going into the discussion on the observations made with all-sky imaging, we briefly describe here the tidal effects on the background temperature profiles. Tidal signatures in temperatures were often reported from resonance lidar studies probing mesospheric altitudes (Li et al., 2005c; Zhao et al., 2003). The thermal inversion layers occurring at the upper mesospheric altitudes (in and around airglow altitudes) are stable and long-lived features that are believed to be formed as a result of tidal interactions with gravity waves (Meriwether and Gardner, 2000, 2004). The temperature profiles measured at 13:55 UT and 22:50 UT on this night (see Fig. 3a) showed signature of a wave-like perturbation with ~20 km vertical wavelength between 70 and 105 km altitudes. From Fig. 3a, it may be noticed that the entire perturbation appears to descend downward with time. The estimated rate of downward phase propagation was ~1 km/h. Such a descent rate with approximately 20-km vertical wavelength is consistent with the signature of the diurnal tide (Forbes, 1995). We may conclude then that the thermal inversions observed at the upper mesospheric region on this night were associated with the passage of the diurnal tide. Such stable thermal inversion layers around airglow altitudes have the potential to act as a duct channel favoring propagation of gravity waves over large horizontal distances and/or evolution of bore-like wave systems.

3.1. Evidence for the presence of medium frequency waves

It was difficult to detect any relatively large-scale medium frequency waves in the image data from the present site due to the vehicular light disturbance emanating from the west. This limits a detailed analysis of any intensity variations occurring at large-scale sizes. Therefore, we utilized intensity averages over a selected pixel area (13 × 13 pixels) from the overhead sky. The resulting time series is analogous to data from a narrow field-of-view photometer. The zenith intensity averages showed a strong nocturnal variation as can be seen in Fig. 4a. Before examining the data for the presence of large-scale medium frequency waves, we should remove this nocturnal variation. We calculated 2-h running mean for the zenith intensity and considered the smooth variation to represent the nocturnal variation (shown as solid curve in Fig. 4a). It may be noted that the 2-h running mean resembles the modeled nocturnal secular variation presented by Huang and Hickey (2008). This slow nocturnal zenith intensity variation was then removed in the zenith intensity data resulting in an intensity time series that revealed medium frequency (0.5–4 h) fluctuations.

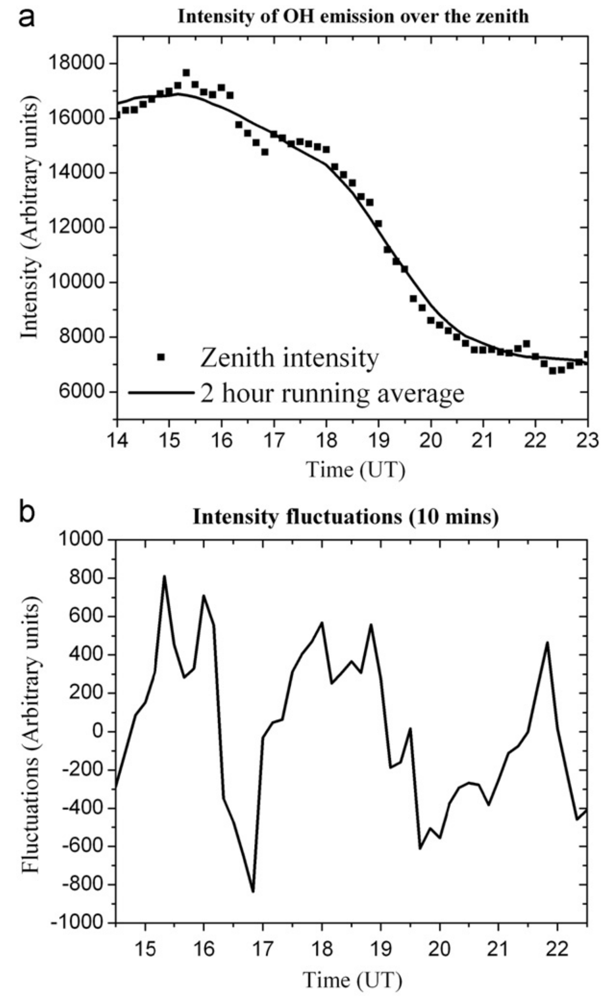

Fig. 4. (a) Typical nocturnal variation of overhead OH emission intensity. The line shows 2 h running average for zenith intensity averages. (b) Residuals resulting from the removal 2 h running average from the nocturnal variation of emission intensity.

Fig. 4b depicts the intensity values with 10-min temporal resolution resulting from the difference between the 2 h running mean and that of the zenith intensity values. It indicates the signature of a medium frequency wave with time period of ~3 h over which some high frequency fluctuations were superposed. The reason for such medium frequency waves not being well resolved in all-sky images is that their horizontal wavelengths were likely to be around or greater than the length scale covered by the field-of-view of the instrument (~360 km at OH altitudes for 130° field-of-view). For the observed time period of ~3 h, waves of horizontal wavelength of 360 km or greater would then have apparent phase speeds of ~33 m/s or greater.

In addition to this, the 10-min averaged winds from the MF radar showed the presence of fluctuations at dominant periods of ~48, ~64 and ~107 min. The filtered 10-min wind data and their amplitude power spectra for both zonal and meridional directions are shown in Fig. 5a and b, respectively. Currently, we do not have information about the propagation directions, wavelengths and phase velocities of these medium frequency waves.

3.2. Observations of short-period waves

This section describes the shorter scale high frequency gravity waves having periodicities of several minutes observed by the imager. Majority of the observed events were classified as QM gravity waves, which have been observed frequently in the previous imaging studies carried out elsewhere (e.g., Taylor et al., 1997; Swenson et al., 1999; Suzuki et al., 2004). Fig. 6 shows snapshots of a few of the QM waves observed on this night that appeared as band-like structures in the images. Ripple events were also detected on this night and the results from an analysis of these events are presented in a separate section.

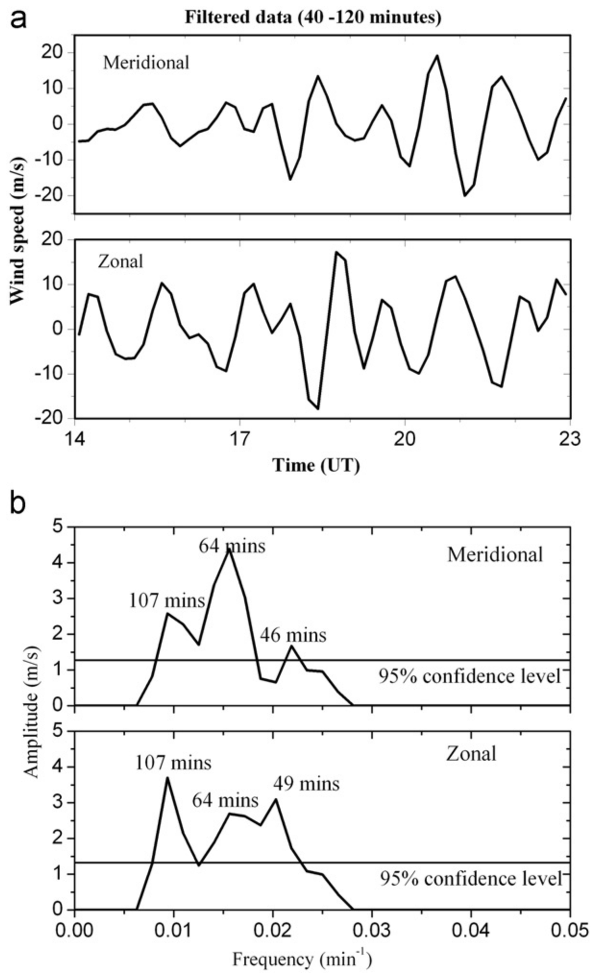

Fig. 5. (a) MF radar zonal and meridional wind data filtered in the period range 40–120 min on the night of February 15, 2007. (b) Amplitude spectra for the winds shown in (a).

We introduce here 'quasi-coherent waves' as those irregular wave-like fluctuations appearing in airglow images whose phase fronts were difficult to follow making the estimation of their wave parameters tedious (in some cases not possible). At the same time, their presence can be detected when the acquired image sequences are seen in motion. Since we are separately discussing the characteristics of QM waves whose parameters were extracted, we use the terminology 'quasi-coherent' to represent the presence of other high frequency gravity waves whose parameters were not derivable.

The waves observed in nightglow imaging are high frequency waves whose periodicities would usually be close to the buoyancy time period. For such waves, if the background vertical wind shears and curvatures are not significant, the dispersion relation can be written as

$$m^2=\left(\frac{N^2}{(c-u)^2}\right)-k^2-\frac{1}{4H^2} \quad \text{or} \quad m^2=\left(\frac{N^2}{\Omega^2}-1\right)k^2-\frac{1}{4H^2} \tag{2}$$

where m and k represent vertical and horizontal wavenumbers, respectively, c and u are the observed phase speed and background wind along the wave propagation azimuth, respectively, H is the scale height ($\sim$6 km), and Ω is the intrinsic wave frequency. There was lack of sufficient data in adjacent altitudes to calculate the wind shears after 19:00 UT. Further, the shears calculated for winds observed between 14:00 and 18:00 UT were less than 8 m/s/km except for a short duration around 18:00 UT. For this reason, we neglect the wind shear and curvature terms in the dispersion relation.

Table 2 lists the estimated parameters for the observed QM wave events. The waves are said to be freely propagating if m^2 is positive (i.e., the vertical wavenumbers are real) from the source region to the observation altitude. The waves are reflected when m^2 becomes negative implying that their vertical wavenumber appearing in the dispersion relation becomes imaginary. The reflection would be partial or total depending on the thickness of the overlying evanescent region. If the evanescent region is thicker than the vertical wavelength of the wave, the reflection would be nearly total. A region of positive m^2 sandwiched between the regions of negative m^2 is actually a wave guide within which the waves get reflected from both above and below. If the resulting interference for a wave is constructive, it would persist. Otherwise, it would perish. Such trapped waves are called ducted waves and it has been inferred from previous studies that the ducted and evanescent waves are indeed efficient enough to perturb nightglow layers significantly (Isler et al., 1997; Simkhada et al., 2009; Snively and Pasko, 2008; Walterscheid et al., 1999).

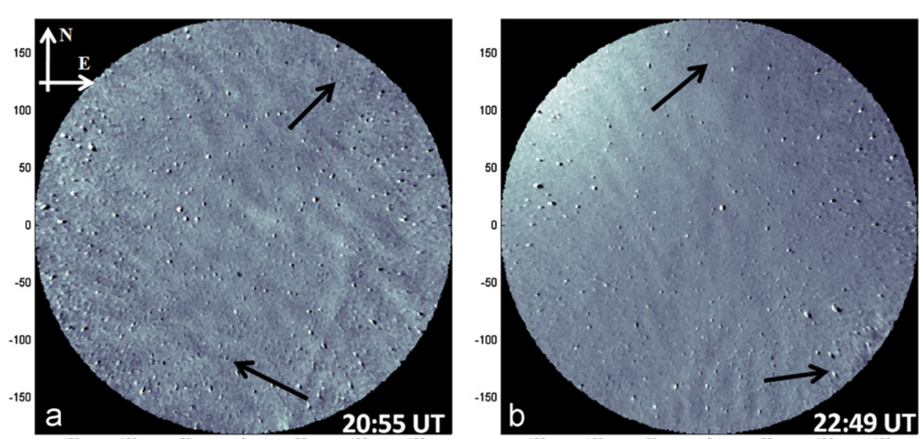

Fig. 6. All-sky airglow images obtained at 20:55 UT and 22:49 UT on the night of February 15, 2007. The arrows indicate the direction of propagation of quasi-monochromatic waves. Events 7 and 8 in Table 2 are shown in Fig. 6a and events 10 and 11 are shown in Fig. 6b.

Table 2
Wave characteristics observed on the night of February 15, 2007.

S.No.	Horizontal wavelength (λ_H), km	Phase velocity (c), m/s	Propagation azimuth, (deg.)	Background wind (u),[a] m/s	m^2 for $N^2=4\times10^{-4}$ rad^2/s^2	Vertical wavelength (λ_Z), km
1.	16.2	55.7	130	14.2	0.075	22.9
2.	20.1	57.1	53	−13.3	−0.024	–
3.	25.5	67.2	76	−8.3	0.003	114.7
4.	14.3 (KH ripple)	25.3	70	−6.6	0.193	14.3
5.	14.5	57.3	93	−3.8	−0.087	–
6.	18.7 (Bore)	37.6	206	−10.3	0.055	26.8
7.	23.5	60.2	46	35.7	0.588	8.2
8.	17.7	34.4	293	−25.9	−0.023	–
9.	13.4	55.0	39	30.4	0.434	9.5
10.	20.5	77.3	62	33.6	0.109	19.0
11.	19.9	76.4	89	37.1	0.152	16.1

[a] The background wind is represented as negative if it is blowing opposite to the direction of propagation of the wave.

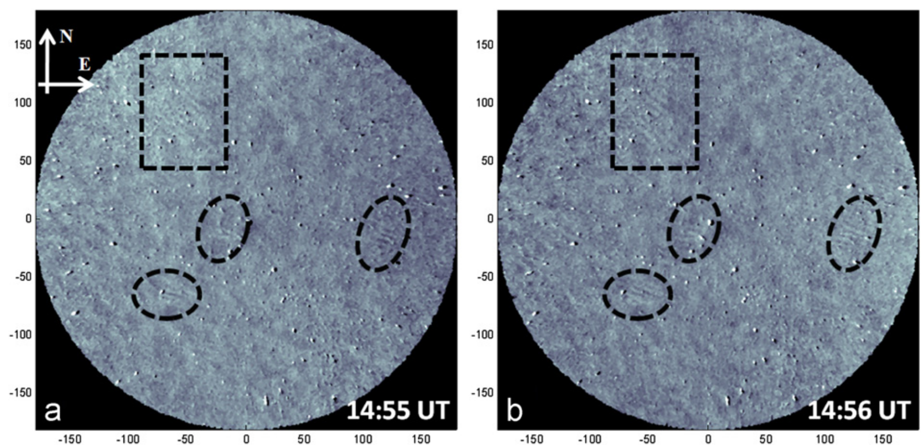

Fig. 7. Airglow images showing convective ripple patches highlighted by squared and circled regions observed at (a) 14:55 UT and (b) 14:56 UT.

The energy difference between the incident and reflected wave components would be carried into the evanescent region, where it would decrease exponentially with height.

From Eq. (2), it can be noted that for high frequency waves m^2 would become negative either if N^2 attains a low value or if the intrinsic wave frequency is greater than the buoyancy frequency. In the high frequency limit, this occurs in the presence of a strong background wind in the direction opposite to that of wave propagation.

In Fig. 3b the regional minima in the N^2 profile attained values as low as $\sim 2\times10^{-4}$ rad^2 s^{-2} on this night. The maximum N^2 in the center of the ducts in the upper mesosphere was $\sim 8\times10^{-4}$ rad^2 s^{-2}. The average value of N^2 in the altitude range 83–91 km for the temperature measurements made at 13:55 UT was 3.2×10^{-4} rad^2 s^{-2} and that for the temperature measurements made at 22:50 UT, it was 4.4×10^{-4} rad^2 s^{-2}. For our discussion, we may consider that for most part of the night the N^2 value was $\sim 4\times10^{-4}$ rad^2 s^{-2} at OH layer altitudes.

In order to ascertain whether the observed waves were freely propagating at airglow emission altitudes, we calculated the m^2 value from the observed wave parameters and background wind for an N^2 value of 4×10^{-4} rad^2 s^{-2} (typical around OH layer). The calculated m^2 values are shown in Table 2. It is found that out of the ten observed QM waves (one event was a KH ripple in the table), seven were freely propagating at the airglow altitudes and the remaining three were evanescent. However, with the current analysis, we could not differentiate between the ducted and freely propagating waves at the airglow altitudes. Interestingly, the vertical wavelength of one of the waves (event no. 3 in Table 2) was very high indicating it was probably approaching a level of reflection and evanescence. In the next section, it will be shown that the vanishing of this wave was accompanied by enhanced wind shear and formation of instability features.

3.3. *Ripple observations*

3.3.1. *Convective ripple observations*

In Fig. 7a and b we depict successive TD images showing several regions marked with oval and rectangular shapes that reveal very short horizontal wavelength features. Their structural appearance suggests that they were ripples. Though no specific QM gravity wave was seen propagating either parallel or perpendicular to these ripples, it could easily be noticed from Fig. 7 that the entire image exhibits several irregular fluctuations. The latter were identified as quasi-coherent waves. Many patches of ripples similar to those in Fig. 7 were frequently seen in the images acquired between 14:15 UT and 15:40 UT. All the observed ripple features propagated towards south-southwest (within 185°–225° azimuths) with wavelengths between 5.0 and 9.5 km. Their phase velocities ranged from 15 to 30 m/s with a mean value of 23.8 m/s. The background mean wind speed between 14:00 and 15:50 UT in the azimuth range 185°–225° was ~19 m/s. This indicates that the ripple features were nearly drifting with the wind. Fig. 8 shows the true wind scatter plot resulting from the individual measurements made between 86 and 90 km altitudes for every hour. The true horizontal wind was found to lie in that part of the quadrant corresponding to east-southeast to south directions during the period of observation of the above mentioned ripples. The wind direction was thus nearly parallel to the alignment of the phase fronts of the ripple features, in conformity with earlier

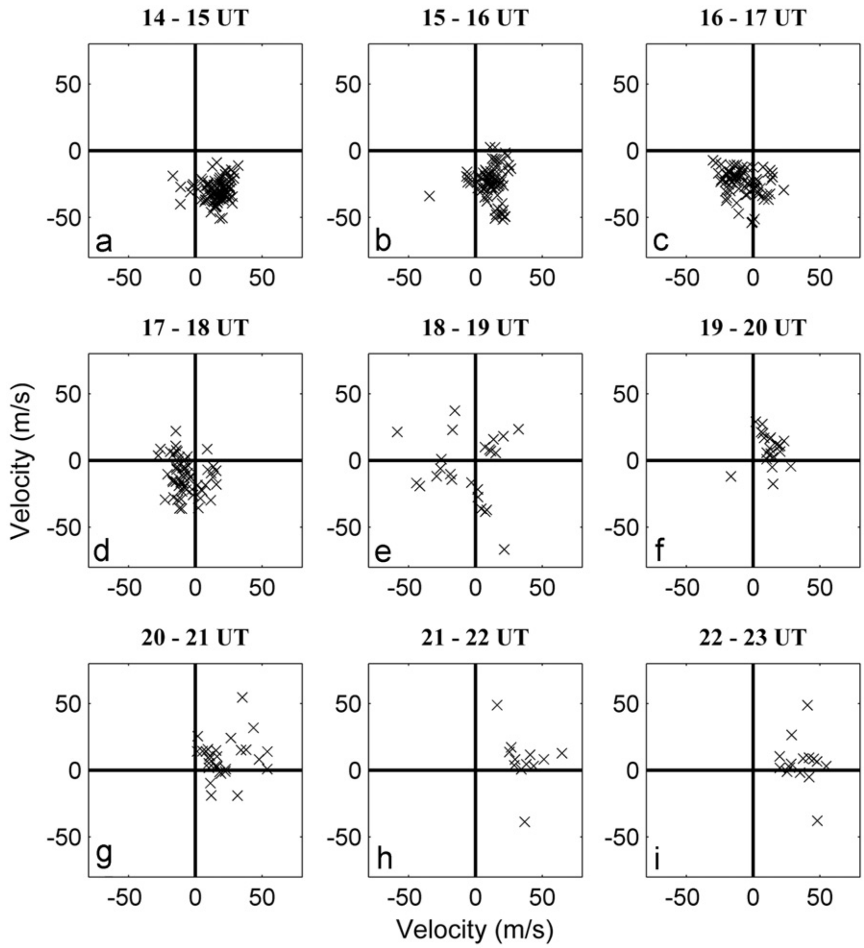

Fig. 8. Hourly polar plots depicting true horizontal wind between 86 and 90 km on the night of February 15, 2007.

reports of convective ripples (Hecht, 2004; Li et al., 2005a; Narayanan et al., 2010).

Fig. 3a reveals a sharp negative gradient of ~8 K/km between 85 and 87 km in the temperature measurements made around 13:50 UT, which was close to the superadiabatic lapse rate of ~9 K/km. In general, the atmosphere is expected to become unstable due to strong temperature perturbations associated with small-scale gravity waves that make the lapse rate superadiabatic. The coexisting quasi-coherent wave features indicate that such waves might have played a role in bringing the atmosphere to convectively unstable state, thereby producing ripples, as discussed in earlier studies (Fritts et al., 1997; Hecht et al., 1997; Yamada et al., 2001; Li et al., 2005a; Narayanan et al., 2010). Also from Fig. 3a, the absence of such a steep temperature gradient at airglow altitudes could be noticed from the measurements made at 22:50 UT and no ripples were observed then. The ripples observed during 14:15–15:40 UT are concluded to be convective in nature and were dominant when there was a steep temperature gradient, as expected according to the theory. Further, they were observed at a time when the temperature gradient was located in the region of OH emission. The noticeable reduction in the frequency of observation of such convective ripples as could be noticed in the images acquired after 16:00 UT is ascribed to the downward motion of the thermal inversion layer.

3.3.2. *Dynamical ripple observations*

Fig. 9a shows a QM wave that propagated towards the east at an azimuth of ~76° (event no. 3 in Table 2). Its horizontal wavelength was found to be ~25 km and the apparent phase velocity was ~67 m/s. Though it appeared faint in individual images, its signature was unmistakable in the images observed between 17:00 and 18:05 UT. Interestingly, in a sequence of images acquired around 18:00 UT, smaller scale wave-like features shown in Fig. 9b were noticed (event no. 4 in Table 2). Their phase fronts were almost parallel to that of the QM wave. From the zonal winds depicted in Fig. 2, it may be noticed that the background zonal wind was westward after 16:00 UT. This indicates that, during the period of the above observation, the QM wave was propagating opposite to the mean flow, which is not unusual for high frequency gravity waves observed by all-sky imaging technique (e.g. Smith et al., 2000). Indeed, this is a condition for which the mean flow will be hindered by a wave propagating in an opposite direction. This might lead to mean flow deceleration, unless otherwise the wave gets reflected. On the other hand, if the mean flow is in the same direction of the wave propagation it is expected to get accelerated. On the night of observations reported herein, shortly after the appearance of the smaller scale features displayed in Fig. 9b, the background wind became very weak. Further, the QM wave signature was not seen afterwards. Thus, the possible role of the mean flow deceleration and weakening due to the QM wave is not to be overlooked. It is also possible that the QM wave might be approaching a level of reflection. The very high vertical wavelength of the QM wave (see Table 2) at the airglow emission altitudes lends credence to this suggestion.

The smaller scale short-lived features appear to be ripples resulting from dynamical instabilities (Kelvin–Helmholtz instabilities) that

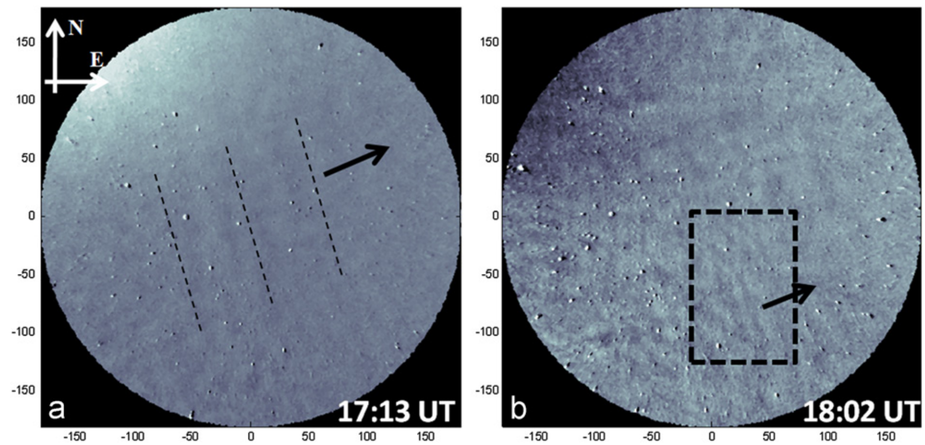

Fig. 9. (a) A time-differenced image showing a QM wave observed at 17:13 UT on February 15, 2007. Three alternate crests of the wave are indicated by dotted lines. (b) Another TD image but observed at 18:02 UT with the box highlighting a ripple feature associated with the wave.

might have been generated by means of wave breaking or wave mean flow interactions. The phase fronts of the QM wave and the shorter scale ripple features were aligned along the same direction and the phase fronts of the ripples were aligned approximately perpendicular to the direction of the mean wind (∼235°). These are in accordance with earlier reports on dynamical ripples (Fritts et al., 1996; Hecht, 2004; Li et al., 2005a, 2005b).

The Richardson number (R_i) is a parameter that defines the balance between the stratification of the atmosphere and its destabilization by means of wind shear as given by the following expression:

$$R_i = \frac{N^2}{(u_z^2 + v_z^2)} \tag{3}$$

where u_z and v_z are vertical shears in zonal and meridional winds, respectively. The condition $0 < R_i < 0.25$ denotes the existence of dynamical instabilities (Hecht, 2004), though there is still an uncertainty regarding the upper limit of R_i and it is argued that dynamical instabilities could occur even if R_i is less than 0.5 (Hines, 1971).

From the foregoing discussion it is clear that for dynamical instabilities to play any role in the formation of observed ripples (event no. 4 in Table 2), there should be enhanced shears in the wind. To examine this aspect with regard to observations presented in Fig. 9, we utilized 20-min averages of wind data available from Tirunelveli and computed the wind shears between sets of two adjacent altitudes sampled, namely, 86–88 km and 88–90 km. The results are plotted in Fig. 10 wherein we notice an enhanced wind shear between 86 and 88 km at around 18:10 UT coincident with the observation of the ripple event described above and shown in Fig. 9. For zonal and meridional wind shears of 21.9 $\mathrm{ms^{-1}\,km^{-1}}$ and 24.2 $\mathrm{ms^{-1}\,km^{-1}}$, respectively, and for N^2 values of $3.2 \times 10^{-4}\,\mathrm{rad^2\,s^{-2}}$ and $4.4 \times 10^{-4}\,\mathrm{rad^2\,s^{-2}}$, we note the corresponding R_i values to be 0.3 and 0.41, respectively. Thus, the short-lived small-scale features shown in Fig. 9 occurred in the presence of enhanced shear in the wind and we infer from their phase front alignments that they were dynamical ripples.

3.4. Observation of a mesospheric bore event

The 'spectacular' gravity wave event observed by Taylor et al. (1995) was interpreted as a mesospheric bore by Dewan and Picard (1998) and they successfully explained most of the observed characteristics of that event. According to their model, mesospheric bores are similar to the hydraulic jumps that occur in shallow water channels. They proposed that strong ducting

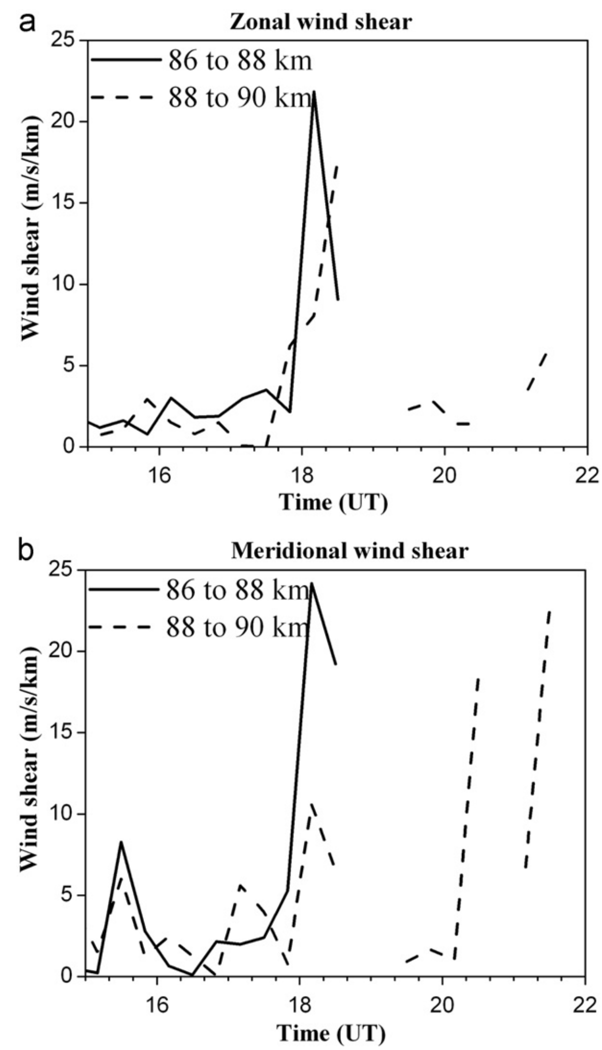

Fig. 10. MF radar derived wind shears computed from 20 minute average wind speeds for the height pairs, 86–88 km and 88–90 km. (a) Shears in zonal wind. (b) Shears in meridional wind.

regions occurring in the mesosphere could act as channels to support evolution of such internal bores. Later, few more reports on mesospheric bores were made available (Smith et al., 2003; 2005; She et al., 2004; Fechine et al., 2005; Medeiros et al., 2005;

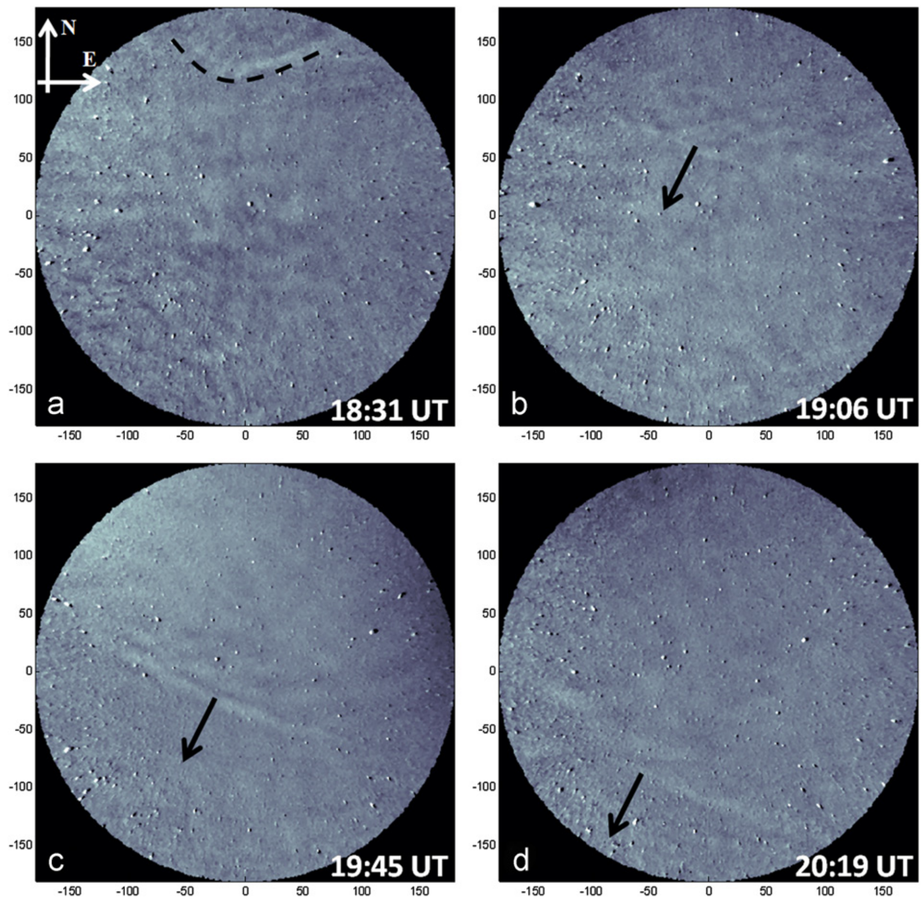

Fig. 11. A sequence of TD images depicting the evolution of a mesospheric bore on the night of February 15, 2007.

Neilson et al., 2006; Stockwell et al., 2006; Narayanan et al., 2009a; Fechine et al., 2009; Yue et al., 2010). Recent simulation studies (Seyler, 2005; Laughman et al., 2009) have shown that the trapping of large-amplitude long-wave perturbations in a duct might result in bore-like non-linearly evolving wave systems inside the duct. It is possible that the ducts themselves arise from a tidal modulation of thermal structure providing favorable conditions for the evolution of bore-like events.

During the night of imaging observations reported herein, a curved bright front entered the field-of-view from the north at 18:24 UT as shown in Fig. 11a. At first the curved front appeared to evolve like an expanding arc, but sooner it was seen as a planar front propagating towards south-southwest direction at an azimuth of 206° as shown in Fig. 11b–d. The frontal structure on the eastward side of the curvature slowly started to disappear by 19:00 UT. The reason for this is not clear. Phase-locked structures then began to evolve behind the leading planar front as expected for mesospheric bores (e.g., Taylor et al., 1995). The trailing undulations were not coherent and long-lived, indicating that the bore might be a foaming bore or mid-way between an undular and a foaming bore analogous to the case reported by She et al. (2004). The measured wavelength and apparent phase velocity, on the average, were ~19 km and ~38 m/s, respectively. The disturbance traversed the overhead sky by 19:35 UT and there was a reversal in the observed background wind around that time (see Fig. 2). The apparent phase speed of the bore appears to be less than that reported in many of the case studies carried out with mesospheric bores. It may be noted that the important condition for bores is that their phase velocity should be higher than the background wind speed or they should propagate in a direction opposite to that of the background wind. In our case, the bore was found to propagate opposite to the direction of the background wind. Further, it is worth noting that Fechine et al. (2005) studied 64 bore-like events from Brazil and found that the apparent phase velocities were in the range 10–70 m/s.

Fig. 12 shows the cross-sections taken from the TD images perpendicular to the propagating front during the course of its evolution. It depicts steepening of the leading front and the propagation of trailing wave crests. Such steepening of the leading front resulting in hydraulic jump-like feature and successive generation of wave crests are well known characteristics of mesospheric bores (Seyler, 2005; Laughman et al., 2009; Neilson et al., 2006; Yue et al., 2010). This also indicates that we are witnessing the early phase of evolution of a bore disturbance in the mesosphere.

It may be recalled that whenever the background wind speed is equal to the phase speed of the wave, the wave ceases to propagate along that direction as a result of critical level absorption. The background wind component was found to be less than 10 m/s along all the directions (see the scatter of winds in Fig. 8e) during the period when a part of the front disappeared. Therefore, critical level absorption was not the reason for partial disappearance of the front along certain directions. Also from Fig. 8e, it may be noticed that the wind motions were highly scattered over several directions during this period. Hence, the background wind alone cannot be responsible for the partial disappearance of the front.

In the earlier reports of mesospheric bores, the sudden rise or fall of intensity of nightglow emissions associated with the passage of bore front assumed primary importance (Taylor et al., 1995; Smith et al., 2003; She et al., 2004). Later on, with theories focusing on the steepening of an initial perturbation in

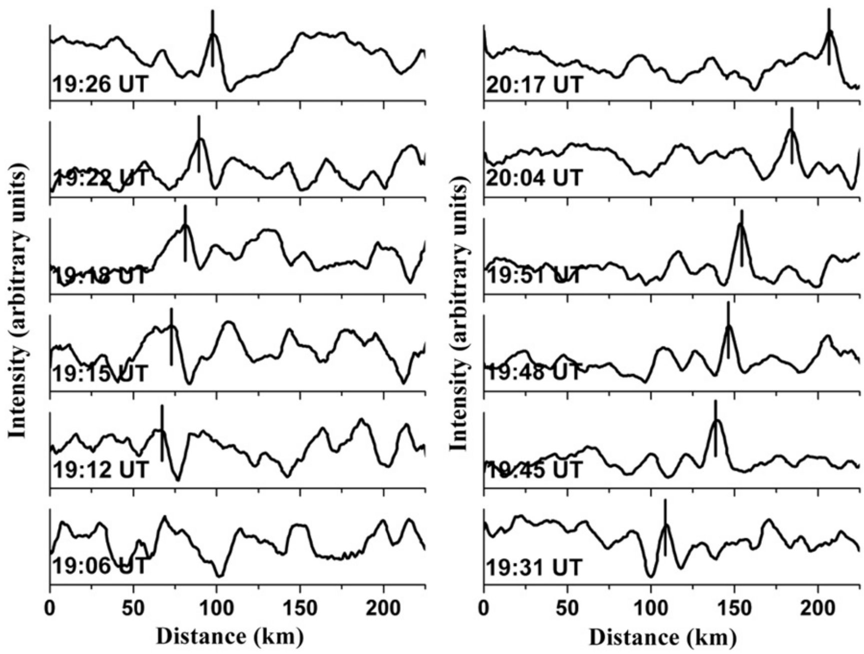

Fig. 12. Cross-sections of intensities orthogonal to the direction of propagation of the bore (extracted from TD images of OH emission). The short vertical lines indicate the position of the leading front.

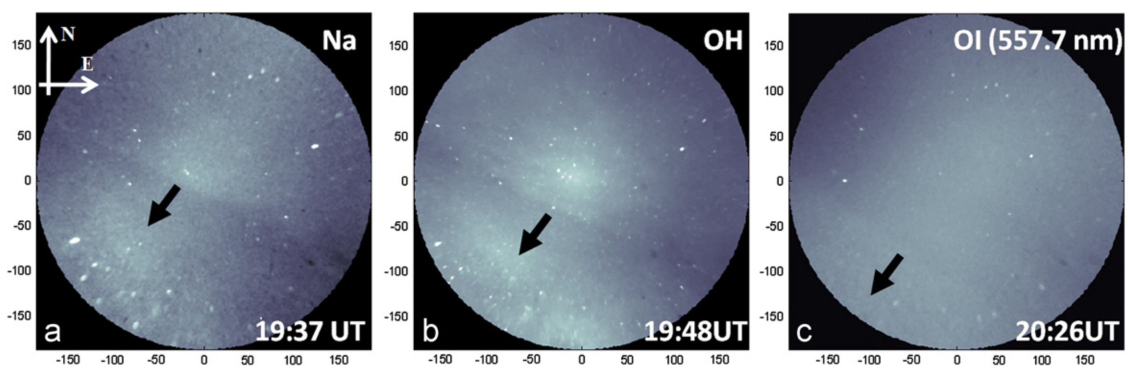

Fig. 13. The signature of the mesospheric bore as observed in raw all-sky images obtained for (a) Na, (b) OH and (c) OI emissions.

the duct (Seyler, 2005; Laughman et al., 2009), the morphology of evolving structures behind the front started gaining more attention (Smith et al., 2003; Nielson et al., 2006; Yue et al., 2010). It is not necessary that all such non-linearly evolving structures should have pronounced intensity variations in the observed emissions. The abrupt intensity variation is supposedly dependent on a variety of parameters like the exact location of the duct with respect to the emission in which it is observed, strength of the initial longwave perturbation and the effectiveness of the perturbation in manifesting itself in the airglow layer.

In the present analysis the bore was observed during a period when the background intensity was falling steeply as could be seen in Fig. 4a. Even then, the bore was observed in OH and Na emissions as a region of enhanced intensity behind the leading front. The disturbance was not seen in OI 557.7 nm emission until about 20:25 UT. In the four OI images acquired from 20:24 to 20:32 UT, a dark feature was noticed accompanying the bright features observed in OH and Na as could be noticed in Fig. 13. Fig. 14 shows the cross-sections extracted across the bore front from a set of observed images. The plots in Fig. 14 were phase shifted to the time of observation of OI 557.7 nm image. The anti-correlation of OI emission with Na and OH emissions and correlation between Na and OH emissions could be clearly seen

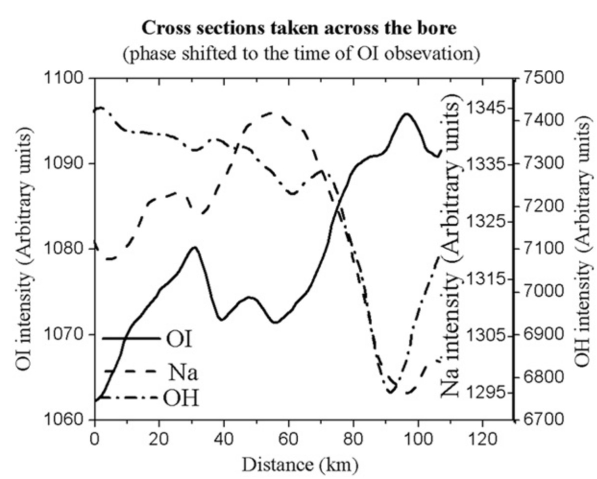

Fig. 14. Cross-sections of intensities taken across the bore front from different airglow emissions.

in the plot. Therefore, it is clear that the intensity variations were in phase between OH and Na images and there was an out-of-phase relationship with the feature noticed in OI 557.7 nm emission. This is called the complementarity feature of mesospheric bores and is in accordance with many of the previous reports of mesospheric bores (e.g. Taylor et al., 1995). The trailing undulations were not clearly resolved in the Na and OI images, but the TD images showed their presence in Na images.

According to Dewan and Picard (1998) model of bores, the emission layers above (below) the duct should be slightly pushed into higher and (lower) colder (hotter) region resulting in less (more) intensity in the airglow emissions. This results in the observed complementarity feature. In the present case the duct might have been situated between Na and OI layer centroid altitudes.

Many of the previous studies had shown that the thermal ducts often support bore development (She et al., 2004; Smith et al., 2005, Narayanan et al., 2009a). Till now only one bore event was attributed to a Doppler duct (Fechine et al., 2009), despite the fact that there was also a noticeable thermal ducting structure. According to theories (Dewan and Picard, 2001; Laughman et al., 2009; Seyler, 2005), both Doppler and thermal ducts and their combinations could support bore formation and evolution. On the other hand, little is known of the horizontal extent of the Doppler ducts and their temporal sustainability. Indeed, it is doubtful that the wind structure would be stable enough at the mesospheric altitudes to form Doppler ducts over a large horizontal extent sustainable for few hours. In contrast, it is now well known that thermal inversions often occur at upper mesospheric altitudes (Meriwether and Gerrard, 2004). They are strong, spatially extended and long lived. In the present work the measured temperature profiles both near the start and end times (13:55 UT and 22:50 UT, respectively) of nightglow observations show the presence of strong inversion layers in the vicinity of OH emission altitudes. On the other hand, the wind field was very weak during the evolution of the observed bore event and there was a wind reversal when the bore disturbance traversed the zenith of the observation location. It is highly unlikely that there was a strong Doppler duct sustaining for more than two hours. Hence, we reason the thermal duct to be the supportive environment for the bore event. If proper allocation is made for the downward tidal progression in the temperature profile of 22:50 UT, a thermal duct may be inferred between the typical Na and OI emission centroids (see Fig. 3a and b) supporting our above reasoning that the thermal duct played a dominant role in the evolution of the observed bore event.

3.5. On the possible source from convective activity

In tropical regions, convective activity is believed to be an important source of gravity waves especially in the high frequency range (Nakamura et al., 2003; Brown et al., 2004). We examined whether convective forcing generated the observed high frequency waves on the night of February 15, 2007 with the aid of OLR data and cloud images obtained by Indian meteorological satellite, Kalpana 1. The OLR contour map is shown in Fig. 15 and satellite images for different times of the day in Fig. 16. Both the OLR and satellite images reveal similar information on convective regions. Mesoscale convective systems were situated to the southwest, southeast and northeast of the observation location each over a distance greater than 1500 km. Since most of the waves at mesospheric heights were seen propagating to the northeast and east, we assessed whether the convective complex in the southwest played any role in generating the waves observed in the all-sky images. The nearest mountain ranges to the observation location are the Western Ghats that are spread along the western coast of the Indian peninsula. However, the higher intrinsic phase speeds of the observed waves rule out the possibility of the direct forcing from orography.

The waves generated in the lower atmosphere would reach the upper atmosphere only if they overcome the wind filtering effects in the middle atmosphere. Here, we utilize the assimilated winds from UKMO to probe the role of wind filtering. The winds were available up to an altitude of $\sim$55 km and we used winds averaged over $10^\circ \times 10^\circ$ latitude–longitude bin centered over the nearest location (9°N, 77°E) and also for the locations of convective complexes situated in southwest (10°S, 55°E) and southeast (10°S, 90°E) directions.

Blocking diagrams show the minimum phase velocity required by a wave to propagate to higher altitudes in specified directions. The waves, whose phase velocities fall inside the blocking region, will be absorbed by means of critical level interactions. Also, inferring the filtering effects from the winds over the observation

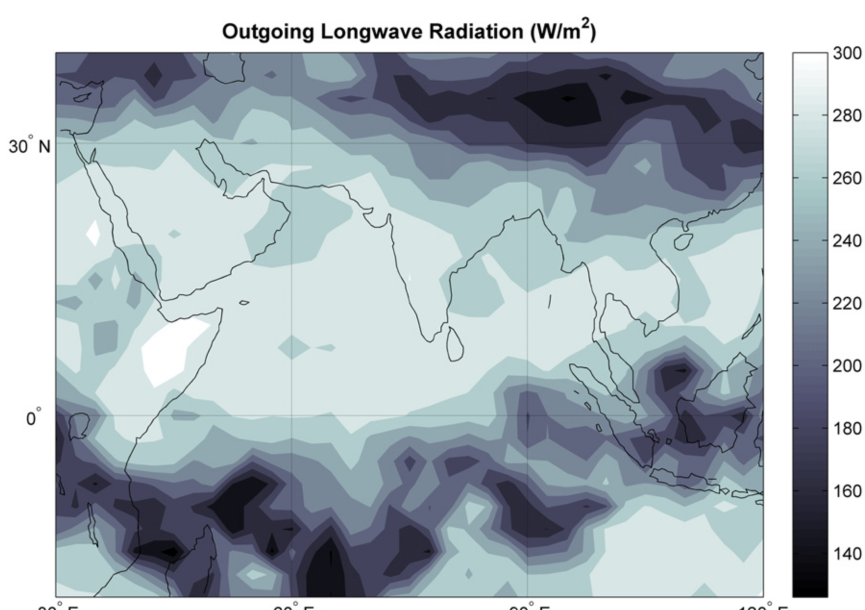

Fig. 15. Contour plot of daily OLR for February 15, 2007.

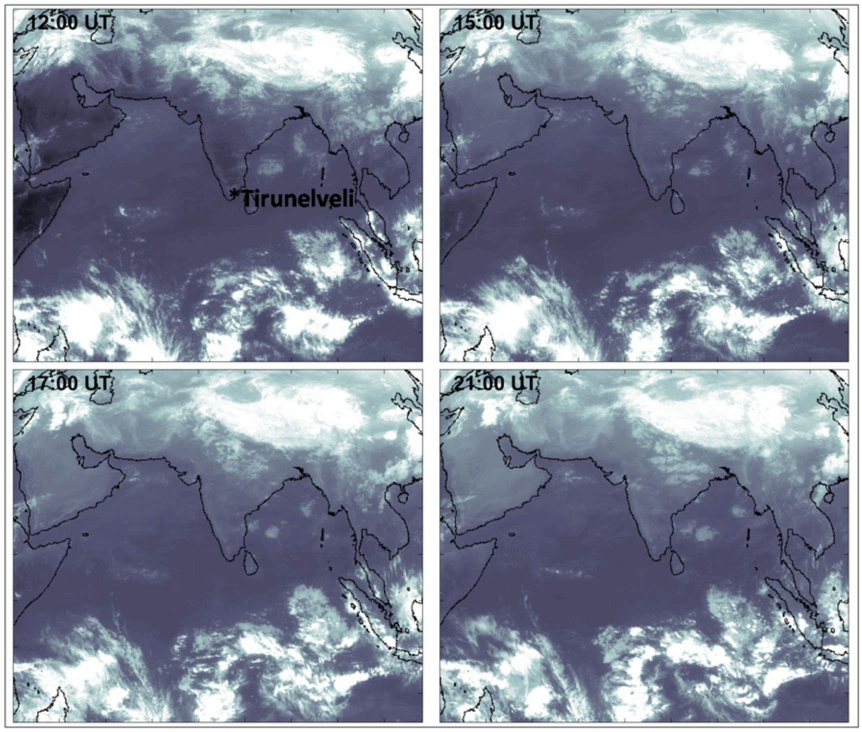

Fig. 16. The cloud images from Indian meteorological satellite, Kalpana 1 on February 15, 2007.

location may not necessarily give the correct inference, whereas wind filtering or blocking shown over an anticipated source region may be more relevant.

The blocking diagrams derived from the UKMO data sets and the observed wave events (indicated by lines terminated by stars) are shown in Fig. 17a, b and c. Fig. 17a shows the effect of wind filtering for the winds centered near Tirunelveli. Fig. 17b and c shows the same for the winds centered over the convectively active zone in the southwest and the southeast directions, respectively. It is clear that the waves propagating towards the northeast were not filtered out by the middle atmospheric winds at least up to the height of the stratopause. Only one wave event (event no. 8 in Table 2) was observed to propagate towards the northwest in airglow images. The blocking diagrams for winds over the convectively active location in the southeast indicate that waves with similar phase speed and direction would be filtered out below stratopause altitude.

Though most of the waves propagating towards northeast support the view that they might have got generated in the convective complexes situated to the southwest, it should be noted that their scale sizes were too short to travel $\sim$1500 km before reaching the upper mesospheric altitudes. Mesospheric ducts or few reflections between lower thermospheric duct and upper troposphere (where there will be sharp gradient in the N^2 profile) might have played a role in their propagation up to and beyond the observation location. It is also possible that these dynamical features could have been secondary waves generated as a result of breaking of relatively large-scale primary waves probably generated by the convectively active regions (Snively and Pasko, 2003; Vadas et al., 2003). A detailed study of these aspects is possible with the help of complex ray tracing analysis incorporating reflection effects. Such an analysis is beyond the scope of this work. Here, we point out that at least a part of the observed waves might have had their sources located in the convectively active region situated about $\sim$1500 km southwest of the observing site.

Although there was significant convective activity occurring on the leeward side of Himalayan range in the northeast direction, it would not have contributed to the high frequency waves on this night because that region lies in the extra-tropical zone and the subtropical tropospheric jet stream could filter out the gravity waves generated there. Though jet streams are believed to generate gravity waves in a wide spectral range, the high frequency gravity waves generated by them are supposed to be predominantly zonal in their phase propagation. It is therefore not possible to detect such waves from the current observation location, which is situated southward of subtropical jet stream.

4. Summary and conclusions

Though there were nights with increased wave activity than the usual level, the night of February 15, 2007, over Tirunelveli was special in that it recorded a variety of different types of dynamical events observed with the all-sky imager. The temperature profiles obtained from SABER/TIMED instrument suggest that the diurnal tide played an important role in determining the mesospheric temperature structure over the observation location on that night and generated persistent thermal ducts in the upper mesospheric region. The presence of medium frequency waves of time periods in the range 0.75–3 h was inferred from the radar winds and zenith intensity time series of images. Our analysis showed that seven out of the ten QM wave events observed on this night were in propagating mode at OH airglow altitudes. The preferred direction of wave propagation on that night as noticed in airglow images, the location of the convective complexes in the lower atmosphere and the filtering effects due to stratospheric winds all together indicate that the convective activity situated towards the southwest of the observation site could have been a potential source of the observed wave activity at mesospheric altitudes. Much of the ripple observations made on this night resemble earlier reports. One noticeable feature that stands out in

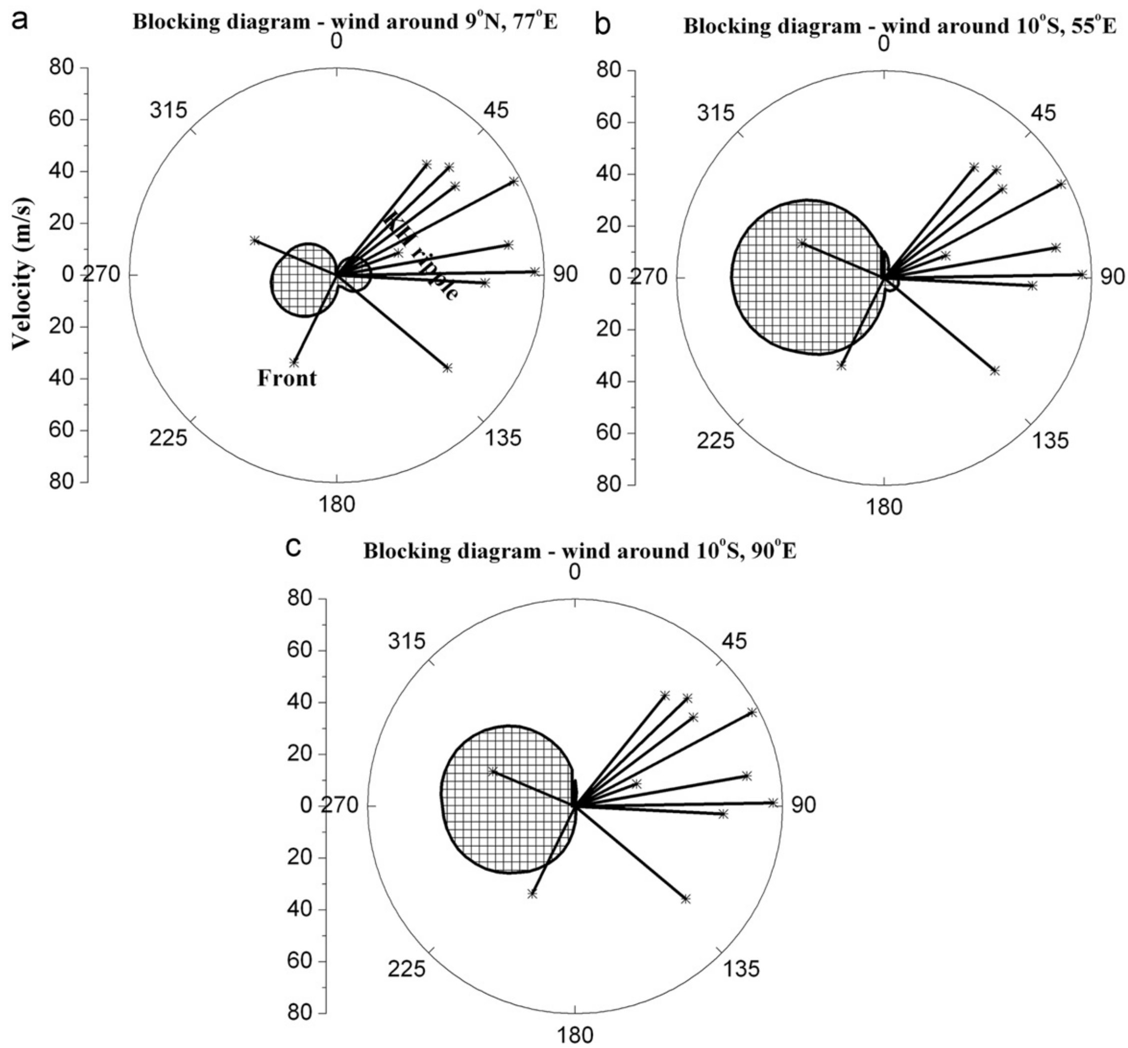

Fig. 17. Blocking diagrams up to the stratopause altitudes derived from UKMO assimilated wind and observed wave events. (a) Blocking diagram for 10° × 10° latitude longitude averaged UKMO winds over Tirunelveli. (b) and (c) Same as (a) but for winds over the location in the southwest direction (10°S, 55°E) and the southeast direction (10°S, 90°E).

these observations is the first time inference of a dynamical ripple in imaging observations made in the Indian region.

One of the observed events showed an early stage of evolution of a frontal system which does support the recent theories on evolution of mesospheric bores (Laughman et al., 2009). Similar to few of the earlier reports (She et al., 2004; Nielson et al., 2006), the trailing wave fronts vanished before the leading front started to fade. The wind field in the upper mesosphere was weak during the bore observations and there was a wind reversal when the bore front crossed the overhead sky of the observation location. The bore appears to have evolved in a thermal duct situated between Na and OI emission centroid altitudes. There are a few unresolved issues with this bore event. The leading front was curved when it entered the field-of-view of the imager possibly indicating some unidentified nearby source. Soon after it entered the field-of-view of the imager, a part of the curved front started to disappear. Analysis of background wind data revealed that the background wind could not have resulted in the suppression of the front in some directions. We are unable to determine the potential source for the bore event and the reason for the suppression of a part of the front.

One of the shortcomings of the airglow data used in this work has been the reduced clarity in the airglow images due to vehicular light contamination on this night of observation. The other shortcomings are the unavailability of continuous data on temperature and high resolution winds. In spite of these limitations, this work is expected to motivate further studies on dynamical phenomena such as mesospheric bore events and small-scale instability features with complementary high resolution wind and temperature data.

Acknowledgments

The authors gratefully acknowledge the SABER team and TIMED mission team for providing useful temperature data sets. The Kalpana 1 satellite images are provided courtesy of University of Wisconsin–Madison Space Science and Engineering Center. The authors also thank the United Kingdom Meteorological Office for providing assimilated winds up to the stratopause. One of the authors (V.L.N.) thanks the Director, Indian Institute of Geomagnetism, for a research scholarship. This work is supported by the Department of Science and Technology, Government of India.

References

Briggs, B.H., 1984. The analysis of spaced sensor records by correlation techniques, in Vol. 13. The Handbook for Middle Atmosphere Program. SCOSTEP Secr., Univ. of IL Urbana, pp. 166–186.

Brown, L.B., Gerrard, A.J., Meriwether, J.W., Makela, J.J., 2004. All-sky imaging observations of mesospheric fronts in OI 557.7 nm and broadband OH airglow emissions: analysis of frontal structure, atmospheric background conditions, and potential sourcing mechanisms. J. Geophys. Res. 109, D19104. doi:10.1029/2003JD004223.

Dewan, E.M., Picard, R.H., 1998. Mesospheric bores. J. Geophys. Res. 103 (D6), 6295–6305.

Dewan, E.M., Picard, R.H., 2001. On the origin of mesospheric bores. J. Geophys. Res. 106 (D3), 2921–2927.

Fechine, J., Medeiros, A.F., Buriti, R.A., Takahashi, H., Gobbi, D., 2005. Mesospheric bore events in the equatorial middle atmosphere. J. Atmos. Sol. Terr. Phys. 67, 1774–1778. doi:10.1016/j.jastp.2005.04.006.

Fechine, J., Wrasse, C.M., Takahashi, H., Medeiros, A.F., Batista, P.P., Clemesha, B.R., Lima, L.M., Fritts, D.C., Laughman, B., Taylor, M.J., Pautet, P.D., Mlynczak, M.G., Russell, J.M., 2009. First observation of an undular mesospheric bore in a Doppler duct. Ann. Geophys. 27, 1399–1406.

Forbes, J.M., 1995. Tidal and planetary waves, in The upper mesosphere and lower thermosphere: a review of experiment and theory. Geophys. Monogr. 87, 67–87.

Fritts, D.C., Isler, J.R., Hecht, J.H., Walterscheid, R.L., Andreassen, Ø., 1997. Wave breaking signatures in sodium densities and OH nightglow 2. Simulation of wave and instability structures. J. Geophys. Res. 102, 6669–6684.

Fritts, D.C., Palmer, T.L., Anderassen, Ø., Lie, L., 1996. Evolution and breakdown of Kelvin–Helmholtz billows in stratified compressible flows. Part 1: comparison of two- and three- dimensional flows. J. Atmos. Sci. 53, 3173–3191.

Garcia, F.J., Taylor, M.J., Kelly, M.C., 1997. Two-dimensional spectral analysis of mesospheric airglow image data. Appl. Opt. 36, 7374–7385.

Hecht, J.H., 2004. Instability layers and airglow Imaging. Rev. Geophys. 42, RG1001. doi:10.1029/2003RG000131.

Hecht, J.H., Walterscheid, R.L., Fritts, D.C., Isler, J.R., Senft, D.C., Gardner, C.S., Franke, S.J., 1997. Wave breaking signatures in OH airglow and sodium densities and temperatures 1. Airglow imaging, Na lidar, and MF radar observations. J. Geophys. Res. 102, 6655–6668.

Hecht, J.H., Walterscheid, R.L., Hickey, M.P., Franke, S.J., 2001. Climatology and modeling of quasi-monochromatic atmospheric gravity waves observed over Urbana Illinois. J. Geophys. Res. 106, 5181–5195.

Hines, C.O., 1971. Generalization of the Richardson criterion for the onset of atmospheric turbulence. Q. J. R. Meteorol. Soc. 97, 429–439.

Hocking, W., 1996. Dynamical coupling processes between the middle atmosphere and lower ionosphere. J. Atmos. Terr. Phys. 58, 735–752.

Huang, T.Y., Hickey, M., 2008. Secular variations of OH nightglow emission and of the OH intensity-weighted temperature induced by gravity wave forcing in the MLT region. Adv. Space Res. 41, 1478–1487.

Isler, J.R., Taylor, M.J., Fritts, D.C., 1997. Observational evidence of wave ducting and evanescence in the mesosphere. J. Geophys. Res. 102, 26,301–26,313.

Laughman, B., Fritts, D.C., Werne, J., 2009. Numerical simulation of bore generation and morphology in the thermal and Doppler ducts. Ann. Geophys. 27, 511–523.

Li, T., She, C.-Y., Williams, B.P., Yuan, T., Collins, R.L., Kieffaber, L.M., Peterson, A.W., 2005a. Concurrent OH imager and sodium temperature/wind lidar observation of localized ripples over northern Colorado. J. Geophys. Res. 110, D13110. doi:10.1029/2004JD004885.

Li, F., Liu, A.Z., Swenson, G.R., Hecht, J.H., Robinson, W.A., 2005b. Observations of gravity wave breakdown into ripples associated with dynamical instabilities. J. Geophys. Res. 110, D09S11. doi:10.1029/2004JD004849.

Li, F., Liu, A.Z., Swenson, G.R., 2005c. Characteristics of instabilities in the mesopause region over Maui, Hawaii. J. Geophys. Res. 110, D09S12. doi:10.1029/2004JD005097.

Medeiros, A.F., Fechine, J., Buruti, R.A., Takahashi, H., Wrasse, C.M., Gobbi, D., 2005. Response of OH, O2, and OI 5577 airglow emissions to the mesospheric bore in the equatorial region of Brazil. Adv. Space Res. 35, 1971–1975.

Medeiros, A.F., Taylor, M.J., Takahashi, H., Batista, P.P., Gobbi, D., 2001. An unusual airglow wave event observed at Cachoeira Paulista 23°S. Adv. Space Res. 27, 1749–1754.

Meriwether, J.W., Gardner, C.S., 2000. A review of the mesosphere inversion layer phenomenon. J. Geophys. Res. 105, 12405–12416.

Meriwether, J.W., Gerrard, A.J., 2004. Mesosphere inversion layers and stratosphere temperature enhancements. Rev. Geophys. 42, RG3003. doi:10.1029/2003RG000133.

Nakamura, T., Aono, T., Tsuda, T., Admiranto, A.G., Achmad, E., Suranto, 2003. Mesospheric gravity waves over a tropical convective region observed by OH airglow imaging in Indonesia. Geophys. Res. Lett. 30, 1882–1885. doi:10.1029/2003GL017619.

Nakamura, T., Higashikawa, A., Tsuda, T., Matsushita, Y., 1999. Seasonal variations of gravity wave structures in OH airglow with a CCD imager at Shigaraki. Earth Planets Space 51, 897–906.

Narayanan, V.L., Gurubaran, S., Emperumal, K., 2009a. A case study of a mesospheric bore event observed with an all-sky airglow imager at Tirunelveli (8.7°N). J. Geophys. Res. 114, D08114. doi:10.1029/2008JD010602.

Narayanan, V.L., Gurubaran, S., Emperumal, K., 2009b. Imaging observations of upper mesospheric nightglow emissions from Tirunelveli (8.7°N). Indian J. Radio Space Phys. 38, 150–158.

Narayanan, V.L., Gurubaran, S., Emperumal, K., 2010. Airglow imaging observations of small scale structures driven by convective instability in the upper mesosphere over Tirunelveli (8.7°N). J. Geophys. Res. 115, D19119. doi:10.1029/2009JD012937.

Nielson, K., Taylor, M.J., Stockwell, R.G., Jarvis, M.J., 2006. An unusual mesospheric bore event observed at high latitudes over Antarctica. Geophys. Res. Lett. 33, L07803. doi:10.1029/2005GL025649.

Rajaram, R., Gurubaran, S., 1998. Seasonal variabilities of low-latitude mesospheric winds. Ann. Geophys. 16, 197–204.

Seyler, C.E., 2005. Internal waves and undular bores in mesospheric inversion layers. J. Geophys. Res. 110, D09S05. doi:10.1029/2004JD004685.

She, C.Y., Li, T., Williams, B.P., Yuan, T., Picard, R.H., 2004. Concurrent OH imager and sodium temperature/wind lidar observation of a mesopause region undular bore event over Fort Collins/Plateville, Colorado. J. Geophys. Res. 109, D22107. doi:10.1029/2004JD004742.

Shiokawa, K., Ejiri, M.K., Ogawa, T., Yamada, Y., Fukunishi, H., Igarashi, K., Nakamura, T., 2003. A localized structure in OH airglow images near the mesopause region. J. Geophys. Res. 108, 4048. doi:10.1029/2002JD002462.

Simkhada, D.B., Snively, J.B., Taylor, M.J., Franke, S.J., 2009. Analysis and modeling of ducted and evanescent gravity waves observed in the Hawaiian airglow. Ann. Geophys. 27, 3213–3224.

Smith, S.M., Friedman, J., Raizada, S., Tepley, C., Baumgardner, J., Mendillo, M., 2005. Evidence of mesospheric bore formation from a breaking gravity wave event: simultaneous imaging and lidar measurements. J. Atmos. Sol. Terr. Phys. 67, 345–356.

Smith, S.M., Mendillo, M., Baumgardner, J., Clark, R.R., 2000. Mesospheric gravity wave imaging at a subauroral site: first results from Millstone Hill. J. Geophys. Res. 105, 27119–27130.

Smith, S.M., Taylor, M.J., Swenson, G.R., She, C.-Y., Hocking, W., Baumgardner, J., Mendillo, M., 2003. A multidiagnostic investigation of the mesospheric bore phenomenon. J. Geophys. Res. 108, 1083. doi:10.1029/2002JA009500.

Snively, J.B., Pasko, V.P., 2003. Breaking of thunderstorm-generated gravity waves as a source of short-period ducted waves at mesopause altitudes. Geophys. Res. Lett. 30, 2254. doi:10.1029/2003GL018436.

Snively, J.B., Pasko, V.P., 2008. Excitation of ducted gravity waves in the lower thermosphere by tropospheric sources. J. Geophys. Res. 113, A06303. doi:10.1029/2007JA012693.

Stockwell, R.G., Taylor, M.J., Nielson, K., Jarvis, M.J., 2006. A novel joint space-wavenumber analysis of an unusual Antarctic gravity wave event. Geophys. Res. Lett. 33, L08805. doi:10.1029/2005GL025660.

Suzuki, S., Shiokawa, K., Otsuka, Y., Ogawa, T., Wilkinson, P., 2004. Statistical characteristics of gravity waves observed by an all-sky imager at Darwin, Australia. J. Geophys. Res. 109, D20S07. doi:10.1029/2003JD004336.

Swenson, G.R., Haque, R., Yang, W., Gardner, C.S., 1999. Momentum and energy fluxes of monochromatic gravity waves observed by an OH imager at Starfire Optical Range, New Mexico. J. Geophys. Res. 104, 6067–6080.

Swenson, G.R., Mende, S.B., 1994. OH emission and gravity waves (including a breaking wave) in all-sky imagery from Bear Lake. Geophys. Res. Lett. 21, 2239–2242.

Swenson, G.R., Qian, J., Plane, J.M.C., Espy, P.J., Taylor, M.J., Turnbull, D.N., Lowe, R.P., 1998. Dynamical and chemical aspects of the mesospheric Na "wall" event on October 9, 1993 during the Airborne Lidar and Observations of Hawaiian Airglow (ALOHA) campaign. J. Geophys. Res. 103, 6361–6380.

Taylor, M.J., Pendleton Jr., W.R., Clark, S., Takahashi, H., Gobbi, D., Goldberg, R.A., 1997. Image measurements of short-period gravity waves at equatorial latitudes. J. Geophys. Res. 102, 26283–26299.

Taylor, M.J., Turnbull, D.N., Lowe, R.P., 1995. Spectrometric and imaging measurements of a spectacular gravity wave event observed during ALOHA-93 campaign. Geophys. Res. Lett. 22, 2849–2852.

Vadas, S.L., Fritts, D.C., Alexander, M.J., 2003. Mechanism for the generation of secondary waves in the wave breaking regions. J. Atmos. Sci. 60, 194–214.

Walterscheid, R.L., Hecht, J.H., Vincent, R.A., Reid, I.M., Woithe, J., Hickey, M.P., 1999. Analysis and interpretation of airglow and radar observations of quasi-monochromatic gravity waves in the upper mesosphere and lower thermosphere over Adelaide, Australia (35°S, 138°E). J. Atmos. Sol. Terr. Phys. 61, 461–478.

Wrasse, C.M., Nakamura, T., Takahashi, H., Medeiros, A.F., Taylor, M.J., Gobbi, D., Denardini, C.M., Fechine, J., Buruti, R.A., Salatun, A., Suratno, Achmad, E., Admiranto, A.G., 2006. Mesospheric gravity waves observed near equatorial and low-middle latitude stations: wave characteristics and reverse ray tracing results. Ann. Geophys. 24, 3229–3240.

Yamada, Y., Fukunishi, H., Nakamura, T., Tsuda, T., 2001. Breaking of small-scale gravity wave and transition to turbulence observed in OH Airglow. Geophys. Res. Lett. 28, 2153–2156.

Yue, J., She, C.Y., Nakamura, T., Harrell, S., Yuan, T., 2010. Mesospheric bore formation from large-scale gravity wave perturbations observed by collocated all-sky OH imager and sodium lidar. J. Atmos. Sol. Terr. Phys. 72, 7–18.

Zhao, Y., Liu, A.Z., Gardner, C.S., 2003. Measurements of atmospheric stability in the mesopause region at Starfire optical range, NM. J. Atmos. Sol. Terr. Phys. 65, 219–232.